SCIENCE CHINA
Physics, Mechanics & Astronomy

•Article•

March 2024 Vol. 67 No. 3: 236113
https://doi.org/10.1007/s11433-023-2291-2

Unveiling the time-temperature dependence of metastability of supercooled liquid using nano-calorimetry

Yijun Ding[1], Lijian Song[2], Zheng Wang[1], Ruiqi Yu[3], Junqiang Wang[2], Lina Hu[1*], Yuanzheng Yue[4*], and Edgar D. Zanotto[5*]

[1] *Key Laboratory for Liquid-Solid Structural Evolution and Processing of Materials (Ministry of Education), Shandong University, Jinan 250061, China;*
[2] *Ningbo Institute of Materials Technology and Engineering, Chinese Academy of Sciences, Ningbo 315201, China;*
[3] *Key Laboratory of Experimental Teratology, Shandong University, Jinan 250061, China;*
[4] *Department of Chemistry and Bioscience, Aalborg University, Aalborg 9220, Denmark;*
[5] *Department of Materials Engineering, Federal University of São Carlos, São Carlos SP 13.565-905, Brazil*

Received September 7, 2023; accepted November 29, 2023; published online February 4, 2024

There is a lack of understanding of both the conversion of an unstable glass into a metastable supercooled liquid (MSL) upon heating and the metastability of MSLs. In this study, we investigated the time- and temperature-dependent metastability of an MSL using an advanced nano-calorimetric technique. The chosen Au-based metallic glass (AuMG) allowed adequate probing of its MSL in a temperature range between 10 and 70 K above the standard glass transition temperature. We found that the survival time of the MSL state is a quadratic function of temperature. Beyond this duration threshold, the sample undergoes fast crystallization even if it is below the crystallization temperature that is measured using differential scanning calorimetry. Employing transmission electron microscopy, we observed the formation of clusters with a partially ordered lattice structure during relaxation in the AuMG sample fabricated using a nano-calorimeter. The atomic ordering within the clusters was enhanced by increasing time and temperature in the MSL region. Once the as-produced glass entered the MSL stage upon heating followed by a quenching stage at a given rate, the mechanical properties of the quenched glass remained the same regardless of its holding temperature and duration within the MSL region. This work provides insights into the glass-MSL-crystal transformation and offers guidance for designing standard metallic glasses for property characterizations.

metallic glass, supercooled liquid, relaxation, nucleation, nano calorimetric technology

PACS number(s): 81.05.Kf, 64.70.Pf, 61.20.Lc, 64.60.Qb

Citation: Y. Ding, L. Song, Z. Wang, R. Yu, J. Wang, L. Hu, Y. Yue, and E. D. Zanotto, Unveiling the time-temperature dependence of metastability of supercooled liquid using nano-calorimetry, Sci. China-Phys. Mech. Astron. **67**, 236113 (2024), https://doi.org/10.1007/s11433-023-2291-2

1 Introduction

A supercooled liquid is a liquid that survives below its freezing point without crystallization [1]. It is structurally disordered, fully relaxed, and metastable against crystallization; whereas glasses are also disordered, but are temporarily frozen, unrelaxed, and thermodynamically unstable [2,3]. Although the dynamic evolution from the supercooled liquid to the glassy state upon cooling has been extensively studied through experiments and computer simulations, the transition phenomenon of glasses back to their metastable

*Corresponding authors (Lina Hu, email: hulina0614@sdu.edu.cn; Yuanzheng Yue, email: yy@bio.aau.dk; Edgar D. Zanotto, email: dedz@ufscar.br)

supercooled liquids (MSLs) upon heating, including the duration of the MSL state, has yet to be clarified [4-9]. The glass forming ability [10], thermoplastic formation ability [11], and mechanical performance [12] of glasses strongly depend on the characteristics of their MSL state. For example, an effective approach to enhance the plasticity of metallic glasses involves initially heating a glass to transform it into an MSL and then rapidly quenching it [13]. Also, the occurrence of viscous flow in supercooled liquids is crucial for enabling the thermoplastic formation of glasses [14,15]. Hence, it is important to precisely identify the structure and dynamics of the MSL region prior to the onset of crystallization [16,17].

Two ubiquitous kinetic processes are observed in glasses and supercooled liquids, namely relaxation and crystallization [18]. It is crucial to understand the correlation between these two processes, because it determines the temperature and time range of existence of MSLs. The classical nucleation theory (CNT) suggests that during heating a glass undergoes relaxation to an MSL state, followed by stochastic formation of critical-sized crystal nuclei through thermal fluctuations [19,20]. The classical view was that the tendency towards crystal nucleation begins only after the MSL is reached. However, a different scenario has been recently proposed as follows. By observing the evolution of the number of crystalline nuclei during a very long treatment time (months) below the glass transition temperature (T_g), it is evident that crystal nucleation starts (more or less) simultaneously with the relaxation process [21,22]. Another indirect evidence is the establishment of steady-state nucleation regime in glasses, which occurs at a much slower rate than that expected from the classical α-relaxation process reflected by changes in the density or refractive index [23,24]. Therefore, monitoring the thermodynamic and dynamic evolutions of glasses during continuous changes in temperature and time prior to crystallization is imperative for elucidating the correlation between relaxation and crystallization, thereby identifying the MSL domain.

The recently developed nano-calorimetric technique offers an extensive range of heating and cooling rates up to 4×10^4 K/s [25] to allow *in-situ* observation of the thermodynamic and kinetic behavior of samples. Simultaneously, this technology offers high precision in the measured thermal signal [26] and excellent time resolution. Therefore, nano-calorimetry enables the *in-situ* investigation of subtle property changes in supercooled liquids by providing detailed thermodynamic and kinetic information about their evolution.

Here, $Au_{50}Cu_{25.5}Ag_{7.5}Si_{17}$ metallic glass (AuMG) and $La_{60}Ni_{15}Al_{25}$ metallic glass (LaMG) were chosen due to their relatively wide supercooled liquid range of approximately 50 K [27]. This temperature range offers a suitable window for probing the evolution of the MSL state [28]. We determined the temperature- and time-dependent range of the MSL region during the transition from glass through supercooled liquid toward crystal. We verified that the relaxation process is accompanied by the formation of clusters with a partially ordered lattice structure, and the ordering degree is slightly enhanced in the MSL region. These findings provide valuable information about the glass-MSL-crystal transformation and guidance for designing glasses with stable and uniform properties.

2 Materials and method

Sample preparation: Metal particles (Au 99.99%, Ag 99.99%, Cu 99.95%, Si 99.95%, La 99.5%, Ni 99.99%, and Al 99.99%) were purchased from ZhongNuo Advanced Material (Beijing) Technology Co., Ltd. The particles were well-mixed at two different nominal compositions ($Au_{50}Cu_{25.5}Ag_{7.5}Si_{17}$ and $La_{60}Ni_{15}Al_{25}$), melted in an electric arc furnace, and then quenched to the glassy state. These metallic systems have a relatively high glass-forming ability; that is, the thickness of the cast glass can exceed 5 mm for the Au-based MG [27] and 12 mm for La-based MGs [29], and the resultant glasses have a relatively high stability against crystallization upon heating. The vacuum degree of the electric arc furnace reached 10^{-4} Pa, and the melt was protected by a high-purity argon (99.999%) atmosphere. This melting process was repeated five times in the furnace to ensure a homogeneous composition. The produced metal ingot was transferred to a quartz tube and fabricated into amorphous ribbons (approximately 30 μm in thickness) using melt-spinning technology under the same atmospheric conditions employed during melting.

Test of thermodynamic properties: Au-based MGs have a relatively low T_g (~400 K [30]). Furthermore, this Au-based MG exhibits high resistance to oxidation [31], ensuring its stable chemical composition even after many scan cycles. These features allowed us to probe the thermodynamic and kinetic properties of the Au-based MG supercooled liquid with high accuracy using nano-calorimetric technology. The nano-calorimetric measurements were performed using a Mettler-Toledo Flash DSC2$^+$ with a UFS 1 chip. A scalpel was used under an optical microscope to cut the metal ribbon into square pieces with a side length of approximately 100 μm, which fit the chip-heating area. The square pieces were carefully transferred to the chip-heating area. To ensure good thermal contact, the pieces were first heated to 673 K (compared with the melting point of 632 K) and maintained at this temperature for 300 s.

Structural characterizations: After the thermodynamic property test, the nano-calorimetric samples were carefully removed from the chips and prepared using focused ion beam technology for TEM analysis. Microstructures of the

samples were observed using an FEI Talos F200X TEM instrument. The acceleration voltage was 200 kV, and the TEM spot resolution was 0.25 nm.

Test of mechanical properties: Mechanical properties of the La-based samples were tested *via* nanoindentation experiments using a Hysitron TI 980 (BRUKER, Inc., USA). A triangular pyramid-shaped Berkovich diamond indenter with a tip curvature radius of 30 nm was used for constant-velocity loading: loading for 5 s, holding for 2 s, and unloading for 5 s. The maximum load was 2000 mN, five points were randomly selected from the clean part of the sample, and the average value was reported.

3 Results

The $Au_{50}Cu_{25.5}Ag_{7.5}Si_{17}$ alloy, which has a liquidus temperature T_L = 632 K, was first heated to 673 K at 100 K/s and then cooled to room temperature at 8000 K/s in a nano-calorimeter (critical cooling rate for glass formation: approximately 600 K/s [28]) to form a fresh MG. Figure 1(a) shows the heat flow curve (black line) of the fresh glass sample upon reheating at 100 K/s. The crossing points of two pairs of tangent lines show a T_g value of 403 K (green dotted lines) and a crystallization onset temperature (T_x) of 473 K (orange dotted lines). The first-order derivative of the differential scanning calorimetry (DSC) curve (red dashed line) shows a maximum between T_g and T_x, which is another characteristic temperature of the glass transition and is denoted as T_g'. It has been reported that the T_g' value obtained this way is more accurate than that determined by the tangent method [32]. To observe the MSL range and its evolution, annealing experiments were conducted using nano-calorimetry at 13 temperatures (T_a, denoted by dots in the black curve in Figure 1(a)) ranging from $0.9T_g$ (slightly lower than the glass transition onset temperature $T_{g,onset}$) to T_x for various times (t_a). After annealing, the samples were cooled to room temperature at different rates h (ca. 10-8000 K/s). Subsequently, the reheating curves were recorded at a heating rate identical to the previous cooling rate. The complete heat treatment process is schematically depicted in the inset of Figure 1(a).

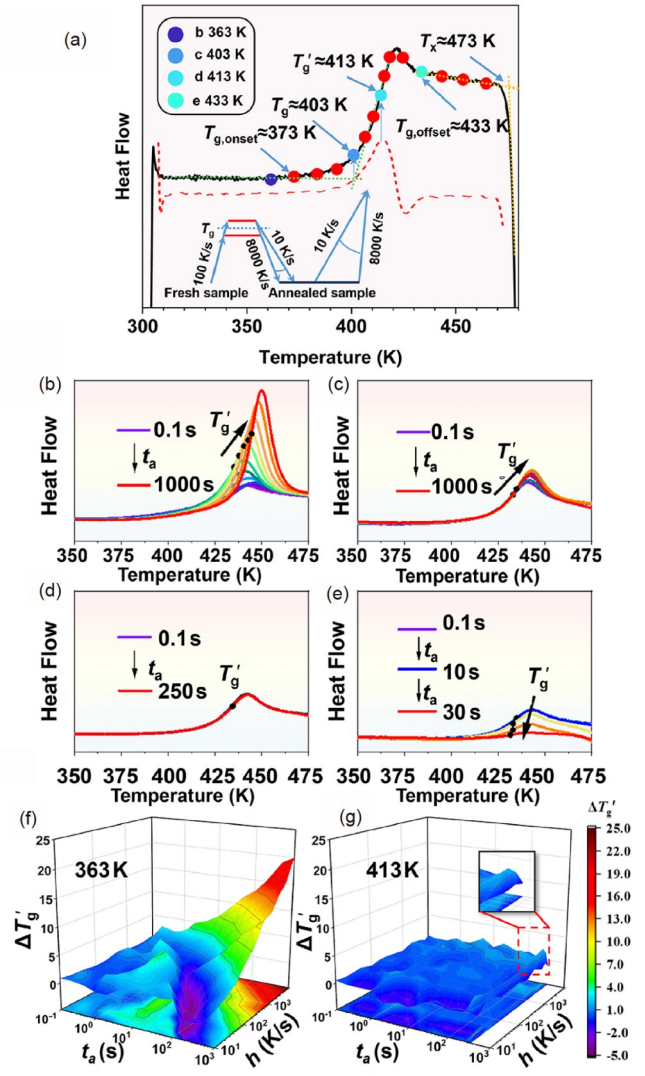

Figure 1 (Color online) Effects of annealing measured by nano-calorimetric technology. (a) Upscan curve obtained at 100 K/s for non-annealed samples (black line) and its first derivative (red dashed line). Filled circles indicate the T_a values. Inset: Heating/cooling protocol. (b)-(e) Curves of samples annealed at four temperatures (scan rate: 1000 K/s). Black dots: T_g' determined for each curve. Black arrows: the changing trend of T_g' with respect to t_a. (f), (g) Change of glass transition temperature ($\Delta T_g'$) as a function of t_a and h at (f) T_a = 363 K and (g) T_a = 413 K.

3.1 Observation of metastable supercooled liquid

The samples annealed for t_a at four temperatures (denoted by various bluish-colored dots in Figure 1(a)) were cooled at 1000 K/s, followed by reheating at the same rate. The nano-calorimetric results are shown in Figure 1(b)-(e). In Figure 1(b), annealing at $0.9T_g$ (363 K) for various t_a leads to the appearance of overshoots above T_g in the reheating curves. With increasing t_a, the intensity of the overshoot increases, and both the overshoot peak and T_g' shift to higher temperatures by up to 16 K. This distinct change in the overshoot peak implies that relaxation proceeds in the glasses with extended t_a [33]. The DSC curves for various t_a values at $0.97T_g$ (393 K) are shown in Figure 1(c), where the endothermic peak is only weakly enhanced, and the peak shifts slightly toward higher temperatures with increasing t_a. At $T_a = 1.03T_g$ (413 K), the overshoot peak remains unchanged when t_a is extended to 250 s (Figure 1(d)). This behavior indicates that the annealing time has no influence on α-relaxation and that the sample reaches a fully relaxed and metastable state at $1.03T_g$ [34]. When T_a further increases (Figure 1(e)), the curves of the first 10 s exhibit the same trend as that in Figure 1(d), i.e., the glass transition peak

remains unchanged. However, as t_a increases to 20-30 s, the glass transition peak becomes weaker and gradually disappears, indicating that crystals form when $t_a > 20$ s. Overall, in Figure 1(b)-(e), we observe three different thermodynamic states from the glass to the supercooled liquid region (i.e., between $0.9T_g$ and T_x): relaxation-driven state (RDS), metastable supercooled liquid (MSL), and crystallite-forming state (CFS).

To further probe these three states, we established a database in which three parameters T_a, t_a, and the reheating rate h (ca. 10-8000 K/s) are variables, and the changes in $\Delta T_g' = T_g'(T_a, \varphi, t_a) - T_g'(T_a, \varphi, t_a = 0.1\text{ s})$ reflect the degree of kinetic fluctuation (Figure 1(f), (g)). The lower the degree of fluctuation, the higher the kinetic stability of the state. Figure 1(f) ($0.9T_g$) shows a distinct dark blue valley and a yellow-red peak, indicating significant fluctuation of $\Delta T_g'$. This also suggests that the glass at $0.9T_g$ is unstable and relaxation proceeds. As a measure of the dynamic heterogeneity, the full width at half maximum (FWHM) of the overshoot peak was also evaluated, because a larger FWHM generally corresponds to a higher degree of dynamic heterogeneity [35]. Figure S1 depicts the change in FWHM of the glass transition peak with regard to t_a at different h values and $0.9T_g$. The FWHM decreases as t_a increases, indicating a significant variation in the distribution of relaxation times, similar to that of $\Delta T_g'$. When T_a reaches 413 K (Figure 1(g)), the overall fluctuation of $\Delta T_g'$ decreases to ±2 K, approaching the limit of error. This indicates that the metastable state is not affected by the heating rate or annealing time. However, there is a drop in T_g' at higher heating rates or longer annealing times (the inset in Figure 1(g), where $t_a \approx 350$ s), which is a signature of the beginning of crystallization. The changes of $\Delta T_g'$ and FWHM at other annealing temperatures are presented in Supplementary Materials.

3.2 Time-temperature boundaries of metastable supercooled liquid

Figure 2 uses the enthalpy (ΔH_g) and activation energy (ΔE_g) for glass transition as metrics to evaluate the time-temperature transformation (TTT) diagram of MSL. The calculation details for ΔH_g and ΔE_g can be found in Supplementary Materials. The evolution trends of ΔH_g with T_a and t_a are depicted in Figure 2(a). The horizontal axis is t_a (from 0 to 1000 s), the left vertical axis is the absolute T_a (from 363 to 473 K), the right vertical axis is the temperature calibrated with T_g (from 0.9 to 1.17 K), and the color represents ΔH_g. Figure 2(a) demonstrates three different thermodynamic states of the supercooled liquids: RDS, MSL, and CFS. RDS lies between 363 and 413 K, while its time window spans from 0 s to a critical t_a. The critical t_a is the time above which ΔH_g remains constant, denoted by the orange dots in Figure 2(a). A significant variation in ΔH_g within this region indicates that the system is under a non-equilibrium state, and the aging effect is experimentally detectable. It is worth noting that this RDS not only exists in the glassy state (below T_g) but also enters the supercooled liquid region (e.g., at $1.03T_g$). This is in line with the simulation work conducted by Wakeda et al. [12], which indicates that the relaxation process of $Cu_{50}Zr_{50}$ continues until it surpasses T_g (approximately $1.1T_g$). The gap between $1.03T_g$ and $1.1T_g$ could be due to the large difference in the heating rate used (100 K/s in our work and 1×10^{12} K/s in ref. [12]). The orange curve in Figure 2(a) was obtained by fitting the experimental data represented by orange dots, resulting in the equation $T_a = 406.64 - 11.35t_a + 0.93t_a^2$). The area above the orange curve is the MSL region. The maximum fluctuation of ΔH_g in the MSL region is less than 1%, indicating that the MSL is thermodynamically stable. When the MSL is heat-treated for a sufficiently long t_a, the crystallites precipitate [36] and then the system enters the CFS region. As a result, the glass transition is affected [37], and the ΔH_g value decreases.

The division of the three regions of supercooled liquids based on ΔE_g is essentially identical to that based on ΔH_g.

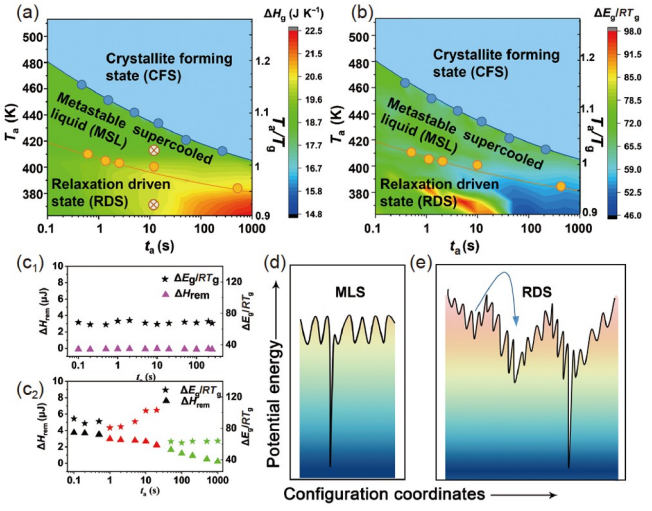

Figure 2 (Color online) Temperature-time-transformation (TTT) diagrams of supercooled liquids and the difference between RDS and MSL in the PEL. (a) TTT diagram of supercooled liquid in terms of the glass transition enthalpy (ΔH_g). (b) TTT diagram of supercooled liquid in terms of the RT_g-scaled activation energy for glass transition ($\Delta E_g/RT_g$), where R is the gas constant. In (a) and (b), the horizontal axis is the annealing time (t_a), the left vertical axis is the annealing temperature (T_a), the right vertical axis is the annealing temperature calibrated with T_g (T_a/T_g), and the color represents the value of ΔH_g or $\Delta E_g/RT_g$. Orange dots: Critical t_a above which ΔH_g remains constant. Blue dots: t_a for initiating crystallization. The orange curve was obtained by fitting the data points represented by orange dots, with the equation $T_a = 406.64 - 11.35t_a + 0.93t_a^2$. The blue curve was obtained by fitting the data points represented by blue dots, with the equation $T_a = 455.95 - 22.85t_a + 1.97t_a^2$. The blue color in the CFS region schematically reflects the small ΔH_g and ΔE_g compared to the other two regions. (c) Changes of H_{rem} (triangles) and ΔE_g (squares) with t_a at 363 K (c$_1$) and 413 K (c$_2$). (d), (e) Schematic PELs drawn based on the changing tendencies of H_{rem} and ΔE_g in both the RDS and MSL. Determination of H_{rem} and ΔE_g is described in Supplementary Materials.

The RDS region exhibits a significant change in ΔE_g with t_a: ΔE_g first increasing from $70RT_g$ to $90RT_g$ and then decreasing to $50RT_g$. Within the MSL region, ΔE_g remains nearly constant, and its fluctuation falls within the error range of the calculated activation energy ($\pm 5RT_g$). The third region (CFS) displays a significantly lower ΔE_g owing to the occurrence of crystallization [37]. Based on Figures 1 and 2, we identify the temperature and time range of MSL based on its constant dynamic and thermodynamic features. As the temperature increases to $1.03T_g$ (413 K), the sample transforms into MSL, and the metastable state can be maintained up to 250 s. As the temperature increases, the duration of this metastable state progressively decreases, sharply declining to 46 s at 423 K and ultimately dropping below 0.5 s at 463 K. The relationship between temperature and MSL duration time can be represented by the equation $T_a = 455.95 - 22.85t_a + 1.97t_a^2$, where $T = 413$-483 K and $t = 0$-250 s (see the blue line in Figure 2(a)). The maximum duration of MSL upon heating (250 s here) is related to the fabrication conditions of glass samples. A higher cooling rate [37] or melting temperature [38] is expected to prolong the MSL retention time. Beyond this threshold time, the supercooled liquid loses its metastability, and crystallization begins. Temperatures represented by the blue line are below T_x (Figure 1) and still within the supercooled liquid region. The response of an amorphous system to an external temperature field can be approximately described by the potential energy landscape (PEL) [39].

Figure 2(c_1) and (c_2) provide an overall view of the correlation between the remanent enthalpy of the sample (H_{rem}) and ΔE_g in MLS and RDS, which was obtained by studying the samples annealed at $T_a = 363$ K ($0.9T_g$) and 413 K. Figure 2(d) and (e) show schematic PELs for the RDS and MSL regions drawn from the evolution of remnant enthalpy (H_{rem}) and ΔE_g with t_a [40,41]. The detailed methods for calculating H_{rem} are described in Supplementary Materials. Figure 2(c_1) shows that, when the long-range flow of atoms is unrestricted in the MLS region ($T_a = 413$ K), H_{rem} and ΔE_g remain unchanged. When t_a equals 0.1 to 250 s, both the valley depth and the energy barrier in the PEL do not change significantly. Figure 2(d) illustrates that within the MSL region, the energy barriers and basin depths between adjacent megabasins exhibit a high degree of consistency. This observation suggests that the local structural units within the MSL region are unable to access the lower basin in the PEL. The kinetic energy at 413 K is sufficient to keep these local units excited, preventing them from absorbing additional energy from the surrounding environment. In contrast, the PEL for RDS (Figure 2(e)) shows very complex changes, with both H_{rem} and ΔE_g exhibiting the following three stages of dependency on t_a (see Figure 2(c_2)). For the short annealing time (<0.5 s), both H_{rem} and ΔE_g decrease slightly, implying that there were inter-sub-basin hopping processes and the system remains in a single mega-basin. At this shortest t_a, only the local loosely packed regions (or flow units) are activated [42,43]. At extended t_a (for $0.5\ \text{s} \leqslant t_a \leqslant 10$ s), the activation energy exhibits a large increase, but H_{rem} remains nearly unchanged. After annealing for more than 20 s, H_{rem} decreases significantly and ΔE_g remains a very small value. This indicates that the atoms have achieved long-range flow, with low activation energies. In the PEL, this stage is represented by atoms jumping from one mega-basin to another and finally reaching the energetically stable positions, as shown in the process represented by the arrow in Figure 2(d). Thus, the second stage ($0.5\ \text{s} \leqslant t \leqslant 10$ s) is the transition of the local atomic motions to long-range cooperative rearrangement [44].

A previous study [45] indicated that long-range flow of locally loose atoms in a glass is achieved through percolation transition. According to the percolation theory, the number of activated flow units increases upon heating [46]. When the proportion of the activated regions is sufficiently large (i.e., it reaches the penetration threshold), the connection between these regions leads to long-range flow [46,47]. In this work, the percolation threshold of flow units is about 29%, which is expressed by the ratio between the enthalpy released via β-relaxation (H_β) at $t_a = 10$ s and the total energy released at 363 K (H_{total}), i.e., H_β/H_{total}. This threshold is close to that found in other metallic glasses, e.g., 25% for $La_{60}Ni_{15}Al_{25}$ [46] and 33% for $Pd_{77.7}Cu_{6.3}Si_{16}$ [48].

3.3 Structural evolution from relaxation driven state (RDS) to metastable supercooled liquid

We also performed transmission electron microscopy (TEM) analysis of two AuMG samples quenched by the nano-calorimetric technique at 8000 K/s to study their nanostructures, as shown in Figure 3. The MSL sample was treated at $T_a = 413$ K for $t_a = 10$ s, while the RDS sample was treated at $T_a = 363$ K also for $t_a = 10$ s (i.e., those marked by the symbol in Figure 2(a)). Figure 3(a) and (b) show high-resolution (HR) TEM images of the two samples, and the insets are the magnified ones. The typical maze-like structure implies the amorphous nature of both samples [49]. Figure 3(c) and (d) show the selected area electron diffraction (SAED) patterns. In addition to the typical diffuse halo SAED patterns of amorphous materials [49], the present glass samples display some bright arcs (marked by the yellow frame). These bright arcs have two implications. Firstly, the bright arcs are related to the degree of order of the matrix. When the sample contains clusters of atoms arranged in an ordered lattice structure, the SAED pattern will display bright spots. The crystalline orientation of these nano-clusters exhibits slight variations within a small angle range, which prevents the bright points from overlapping at specific locations, resulting in the appearance of arcs. The smaller the misorientation between the ordered clusters, the smaller the

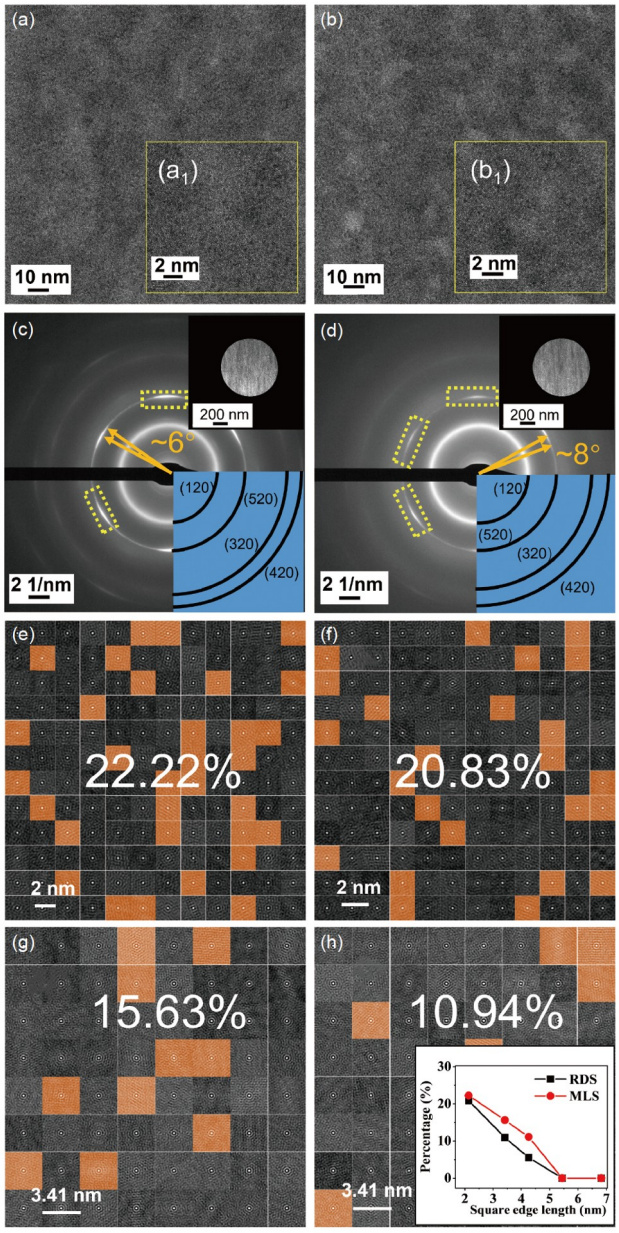

Figure 3 (Color online) HRTEM analysis of samples cooled from MSL and RDS. (a), (b) Images of samples annealed at (a) 413 K and (b) 363 K. Insets (a_1), (b_1) are magnified HRTEM images. (c), (d) SAED patterns of samples annealed at (c) 413 K and (d) 363 K. The insets in the upper right corner of (c) and (d) are the bright field pictures of the samples. The insets in the lower right corner of (c) and (d) are the calibration results of the diffraction arc. (e)-(h) Autocorrelation analysis results after dividing Figure 3(a_1) and (b_1) into 2-nm squares in (e), (g) or 3.41-nm squares in (f), (h). Orange area: ordered region; black area: disordered region. The lower right inset in (h) represents the variation in the proportion of ordered squares with square size. The scalebars for each image can be found in the lower left corner of (a)-(h).

angle of the arc (Figure S6), and hence the higher the degree of matrix order. The maximum difference between the orientations of these clusters is approximately 8° for the sample in the RDS, while that in the MSL state is 6°. A more detailed depiction of this phenomenon is given in Figure S6 of Supplementary Materials. Secondly, by calibrating the radii of the different bright arcs in Figure 3(c) and (d), the ordered clusters in both the RDS and MSL regions are found to be composed of an AuCu-like phase (Figure 3(c) and (d)).

Autocorrelation analysis is an effective method for analyzing the order degree of local atomic packing [50,51]. Here, this method was used to determine the content and size distribution of crystal-like ordered structures formed in the MSL and RDS regions. Figure 3(e)-(h) show the results of autocorrelation analysis obtained after dividing the HRTEM images in Figure 3(a_1) and (b_1) into squares of different sizes. An ordered square area (full of stripes in the image) is marked in orange, and a disordered square area (containing no stripes in the image) is marked in black [52]. The lower-right illustration in Figure 3(f) shows the change in the proportion of ordered squares with square size. The proportion of 2-nm ordered structure is basically the same between the MSL and RDS samples (Figure 3(e) and (g)). At the scale of 3.41-4.26 nm, however, the proportion of ordered structure is significantly higher in the MSL region than that in the RDS region, suggesting that there are more large-scale ordered structures in the MSL. For the square sizes of 5.45 and 6.82 nm, the proportion of ordered clusters decreases to 0, meaning that no crystalloid cluster is larger than 5.45 nm in either MLS or RDS.

According to Schawe and Löffler [37], $Au_{49}Ag_{5.5}Pd_{2.3}Cu_{26.9}Si_{16.3}$ MGs can be categorized into two distinct types. The first type, known as self-doped glass (SDG), involves the formation of quenched in nuclei or nucleated precursors during cooling at 500-4000 K/s. The second type, referred to as chemically homogeneous glass (CHG), does not exhibit quenched nuclei when the cooling rate exceeds 4000 K/s. Based on the method described in ref. [37], different types of MG were identified in the present study, and the results are shown in Supplementary Materials. When the cooling rate is in the range of 600-4000 K/s, crystalline nuclei are generated in the glass during the cooling process. In contrast, when the cooling rate exceeds 4000 K/s, a chemically homogeneous glass without nuclei is obtained. The sample prior to annealing was prepared at a cooling rate of 8000 K/s, and thus the parent glass is chemically homogeneous. Our results imply that even chemically homogeneous glasses could contain some clusters that are smaller than the critical nuclei inherited from the supercooled liquid. During the relaxation process, these clusters gradually form towards the size of about 2 nm, but their orientation is chaotic. Once entering the MSL region, the size and number of clusters gradually increase, and their orientation gradually becomes uniform. After reaching the CFS region, these clusters finally evolve into crystals [53]. This confirms that structural inheritance occurs not only during the liquid-to-glass transition [54,55] but also during the glass-supercooled liquid transition [53,56].

4 Discussion

As mentioned above, the correlation between relaxation and crystal nucleation upon heating glasses is still a matter of debate [57]. No change in the crystallization enthalpy during relaxation was observed for polyamide 6 [58] or Ce-based glass [57]. Considering these results, some researchers believe that crystal nucleation only occurs after full relaxation, whereas other studies show an interplay between the two phenomena [59].

The present study reveals that the relaxation process is accompanied by the generation of clusters with an ordered lattice structure. Note that the crystallization enthalpy is constant in the RDS region, whereas it tends to decrease in the MSL region (Figure S7). The decrease of crystallization enthalpy in the MSL region is mainly related to the long-range translational motion of atoms, as all adjacent megabasins in the PEL are separated by energy barriers of similar heights (Figure 2(c)). Our finding is in line with a previous study [24], which provides an explanation for the frequently reported breakdown of CNT below the temperature of maximum nucleation rate. Based on a detailed analysis of the nucleation rate at low temperatures, Zanotto et al. [21,22] inferred that the process of crystal formation in oxide glasses starts in a non-equilibrium glassy state during the relaxation process and continues in the supercooled liquid state. Our study, by this metallic glass, provides direct evidence supporting this inference.

According to the PEL theory, glasses consist of a plethora of local structures in varying energy states [60-62]. It is impossible to produce a standard glass sample without considering its thermodynamic history. Even glass specimens having the same composition often differ in some of their properties. For example, the fragility index (m) of $Gd_{55}Al_{20}Ni_{25}$ liquid was reported to be 25 in one study [63] and 39 in another study based on the dynamic responses of glasses [64]. It was suggested that the disparity in thermal history between different glass samples could be eliminated simply by heating the sample to a temperature above T_g [65,66]. However, this statement is not accurate based on our present findings. Specifically, Figure 4(a) plots the m values of $Au_{50}Cu_{25.5}Ag_{7.5}Si_{17}$ sample frozen in the RDS and MSL regions. The m value for RDS glass falls in the range of 48-66. For the MSL samples, however, the calculated m values show a relatively small fluctuation (55 ± 2). The intrinsic m value of the glass was calculated using the method outlined previously [67,68], resulting in a m of approximately 57. The calculation procedure is given in Supplementary Materials. This indicates that, upon entering the MSL region, the disparity in thermal history between different glass samples can be effectively erased, and the m is close to the intrinsic value. Figure 4(b) shows the Young's modulus (E) of MGs heat-treated within the RDS and MSL regions. Because the high

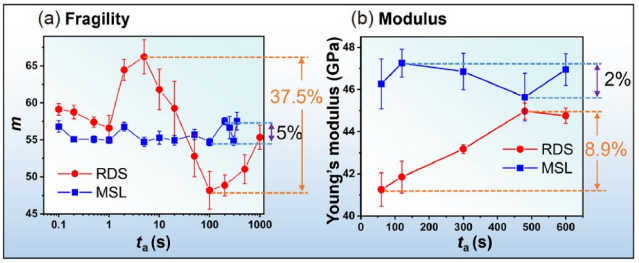

Figure 4 (Color online) Properties of glasses cooled from RDS and MSL. (a) Supercooled liquid fragility of samples annealed at RDS (red circles) and MSL (blue squares) for various t_a. (b) Young's modulus of samples annealed at RDS (red circles) and MSL (blue squares) for various t_a. Vertical bars: experimental errors.

elasticity of Au-based MGs reported in ref. [27] hinders accurate measurement, $La_{60}Ni_{15}Al_{25}$ MGs with moderate elasticity were chosen as the target material instead. Details about the distinction between RDS and MSL for $La_{60}Ni_{15}Al_{25}$ and the specific load-displacement curves from each measurement are provided in Supplementary Materials. The Young's modulus of the representative RDS sample treated at T_a = 413 K exhibits a substantial increase at higher t_a values, with the maximum change reaching approximately 8.9% at t_a = 600 s. This enhancement in mechanical properties could be attributed to a decreased number of flow units (e.g., shear transformation zones) for plastic deformation [69] due to relaxation. In the MSL region (e.g., T_a = 463 K), E remains stable at around 46 GPa, and its fluctuation of approximately 2% is much less than that of the same MG annealed for the same t_a in the RDS region (8.9%) and that of $Cu_{36}Zr_{48}Al_8Ag_8$ MG annealed for 20 min in the RDS region (15.8%) [70]. The uniform properties of samples in the MSL region are attributed to the fact that the PEL of MSL consists of similar valleys. When atoms transition from one valley to another, there is minimal change in energy. This characteristic of the PEL ensures that the sample maintains consistent properties throughout. Our present study demonstrates that, in order to obtain a standard glass from one with an unknown thermal history, it is necessary to reheat the glass to the MSL region before quenching it at a standard cooling rate (e.g., 10 K/min for oxide glasses). This process ensures the achievement of a consistent and reproducible glass structure.

5 Conclusions

We employed the nano-calorimetric technique and TEM analysis to unveil the thermodynamic, kinetic, and structural evolution of an Au-based model metallic glass during heating to the MSL and crystalline states. The temperature and time range of MSL were determined. For this metallic glass, the MSL is located between 10 and 70 K above the glass transition temperature determined by DSC. The duration of

the MSL exhibits a quadratic relationship with temperature. Beyond this duration, the sample will undergo crystallization even if the treatment temperature is below the DSC crystallization temperature.

We observed the formation of clusters with a partially ordered lattice structure during the relaxation process. The ordering degree in the clusters is slightly enhanced during treatment in the MSL region. Annealing in the MSL region effectively eliminates the disparity in thermal history between different glasses (the same composition cooled at different rates), leading to great consistency in Young's modulus.

These findings provide a thorough picture of the relaxation process and shed light on the mechanism behind the transformation of glass into its supercooled liquid state during heating. Furthermore, they highlight the limitations of current relaxation theories and CNT. This work also offers valuable engineering guidance for fabricating a standard glass from one with an unknown thermal history, namely by reheating the glass to the MSL region before quenching it at a standard cooling rate.

We would like to thank Professor Yanfei Zhang from Qilu University of Technology for her help with the flash differential scanning calorimetry experiments. We acknowledge assistance from Shandong University Testing and Manufacturing Center for Advanced Materials in the nanoindentation experiment. This work was supported by the Songshan Lake Materials Laboratory (Grant No. 2021SLABFN05), the National Natural Science Foundation of China (Grant Nos. 51971120, 51901139), the Taishan Scholars Program of Shandong Province (Grant No. tsqn201909010), and the Key Basic and Applied Research Program of Guangdong Province (Grant No. 2019B030302010). Edgar D. Zanotto is grateful to the São Paulo Research Foundation – FAPESP (Grant No. # 2013/07793-6).

Conflict of interest The authors declare that they have no conflict of interest.

Supporting Information

The supporting information is available online at http://phys.scichina.com and https://link.springer.com. The supporting materials are published as submitted, without typesetting or editing. The responsibility for scientific accuracy and content remains entirely with the authors.

1 W. Kauzmann, Chem. Rev. **43**, 219 (1948).
2 M. D. Ediger, C. A. Angell, and S. R. Nagel, J. Phys. Chem. **100**, 13200 (1996).
3 E. D. Zanotto, and J. C. Mauro, J. Non-Cryst. Solids **471**, 490 (2017).
4 C. A. Angell, Science **267**, 1924 (1995).
5 M. D. Ediger, and P. Harrowell, J. Chem. Phys. **137**, 080901 (2012).
6 C. A. Angell, J. Phys.-Condens. Matter **12**, 6463 (2000).
7 F. F. Abraham, J. Chem. Phys. **72**, 359 (2008).
8 L. Berthier, Phys. Rev. Lett. **127**, 088002 (2021).
9 Q. Wang, C. T. Liu, Y. Yang, Y. D. Dong, and J. Lu, Phys. Rev. Lett. **106**, 215505 (2011).
10 Q. Yang, J. Huang, X. H. Qin, F. X. Ge, and H. B. Yu, Sci. China Mater. **63**, 157 (2019).
11 Y. Kawamura, T. Nakamura, and A. Inoue, Scripta Mater. **39**, 301 (1998).
12 M. Wakeda, J. Saida, J. Li, and S. Ogata, Sci. Rep. **5**, 10545 (2015).
13 W. Guo, R. Yamada, J. Saida, S. Lü, and S. Wu, J. Non-Cryst. Solids **498**, 8 (2018).
14 N. Li, Y. Chen, M. Q. Jiang, D. J. Li, J. J. He, Y. Wu, and L. Liu, Acta Mater. **61**, 1921 (2013).
15 G. Ding, F. Jiang, X. Song, L. H. Dai, and M. Q. Jiang, Sci. China-Phys. Mech. Astron. **65**, 264613 (2022).
16 M. D. Ediger, Abstr. Pap. Am. Chem. Soc. **215**, U159 (1998).
17 E. Flenner, H. Staley, and G. Szamel, Phys. Rev. Lett. **112**, 097801 (2014).
18 E. D. Zanotto, and D. R. Cassar, J. Chem. Phys. **149**, 024503 (2018).
19 Z. Wang, F. Wang, Y. Peng, and Y. Han, Nat. Commun. **6**, 6942 (2015).
20 R. P. Sear, J. Phys.-Condens. Matter **19**, 033101 (2007).
21 J. W. P. Schmelzer, T. V. Tropin, V. M. Fokin, A. S. Abyzov, and E. D. Zanotto, Entropy **22**, 1098 (2020).
22 V. M. Fokin, A. S. Abyzov, N. S. Yuritsyn, J. W. P. Schmelzer, and E. D. Zanotto, Acta Mater. **203**, 116472 (2021).
23 A. O. Tipeev, J. P. Rino, and E. D. Zanotto, Acta Mater. **220**, 117303 (2021).
24 L. R. Rodrigues, A. S. Abyzov, V. M. Fokin, and E. D. Zanotto, J. Am. Ceram. Soc. **104**, 3212 (2021).
25 V. Mathot, M. Pyda, T. Pijpers, G. Vanden Poel, E. van de Kerkhof, S. van Herwaarden, F. van Herwaarden, and A. Leenaers, Thermochim. Acta **522**, 36 (2011).
26 C. R. Quick, J. E. K. Schawe, P. J. Uggowitzer, and S. Pogatscher, Thermochim. Acta **677**, 12 (2019).
27 J. Schroers, B. Lohwongwatana, W. L. Johnson, and A. Peker, Appl. Phys. Lett. **87**, 061912 (2005).
28 F. X. Bai, J. H. Yao, Y. X. Wang, J. Pan, and Y. Li, Scripta Mater. **132**, 58 (2017).
29 R. Li, S. Pang, C. Ma, and T. Zhang, Acta Mater. **55**, 3719 (2007).
30 F. X. Bai, J. H. Yao, and Y. Li, Intermetallics **86**, 73 (2017).
31 S. Pogatscher, D. Leutenegger, A. Hagmann, P. J. Uggowitzer, and J. F. Löffler, Thermochim. Acta **590**, 84 (2014).
32 H. B. Yu, Y. Luo, and K. Samwer, Adv. Mater. **25**, 5904 (2013).
33 O. Gulbiten, J. C. Mauro, and P. Lucas, J. Chem. Phys. **138**, 244504 (2013).
34 J. Q. Wang, Y. Shen, J. H. Perepezko, and M. D. Ediger, Acta Mater. **104**, 25 (2016).
35 Z. Lu, B. S. Shang, Y. T. Sun, Z. G. Zhu, P. F. Guan, W. H. Wang, and H. Y. Bai, J. Chem. Phys. **144**, 144501 (2016).
36 D. Okai, Y. Shimizu, N. Hirano, T. Fukami, T. Yamasaki, and A. Inoue, J. Alloys Compd. **504**, S247 (2010).
37 J. E. K. Schawe, and J. F. Löffler, Nat. Commun. **10**, 1337 (2019).
38 Q. Cheng, Y. H. Sun, J. Orava, and W. H. Wang, Mater. Today Phys. **31**, 101004 (2023).
39 P. F. Guan, B. Wang, Y. C. Wu, S. Zhang, B. S. Shang, Y. C. Hu, R. Su, and Q. Liu, Acta Phys. Sin. **66**, 176112 (2017).
40 C. Liu, P. Guan, and Y. Fan, Acta Mater. **161**, 295 (2018).
41 Y. Fan, T. Iwashita, and T. Egami, Phys. Rev. Lett. **115**, 045501 (2015).
42 L. Song, W. Xu, J. Huo, J. Q. Wang, X. Wang, and R. Li, Intermetallics **93**, 101 (2018).
43 R. Xue, L. Zhao, Y. Cai, J. Yi, J. Cheng, P. Wen, W. Wang, M. Pan, and H. Bai, Sci. China-Phys. Mech. Astron. **65**, 246111 (2022).
44 L. T. Zhang, Y. J. Duan, D. Crespo, E. Pineda, Y. J. Wang, J.-M. Pelletier, and J. Q. Qiao, Sci. China-Phys. Mech. Astron. **64**, 296111 (2021).
45 W. H. Wang, Y. Yang, T. G. Nieh, and C. T. Liu, Intermetallics **67**, 81 (2015).
46 Z. Wang, B. A. Sun, H. Y. Bai, and W. H. Wang, Nat. Commun. **5**, 5823 (2014).
47 Z. Wang, P. Wen, L. S. Huo, H. Y. Bai, and W. H. Wang, Appl. Phys. Lett. **101**, 121906 (2012).
48 H. Wagner, D. Bedorf, S. Küchemann, M. Schwabe, B. Zhang, W. Arnold, and K. Samwer, Nat. Mater. **10**, 439 (2011).

49 J. Shen, Z. Lu, J. Q. Wang, S. Lan, F. Zhang, A. Hirata, M. W. Chen, X. L. Wang, P. Wen, Y. H. Sun, H. Y. Bai, and W. H. Wang, J. Phys. Chem. Lett. **11**, 6718 (2020).
50 Y. Wu, H. H. Wu, X. D. Hui, G. L. Chen, and Z. P. Lu, Acta Mater. **58**, 2564 (2010).
51 G. Y. Fan, and J. M. Cowley, Ultramicroscopy **17**, 345 (1985).
52 Q. Wang, C. T. Liu, Y. Yang, J. B. Liu, Y. D. Dong, and J. Lu, Sci. Rep. **4**, 4648 (2014).
53 L. J. Song, M. Gao, W. Xu, J. T. Huo, J. Q. Wang, R. W. Li, W. H. Wang, and J. H. Perepezko, Acta Mater. **185**, 38 (2020).
54 W. Chu, J. Shang, K. Yin, N. Ren, L. Hu, Y. Zhao, and B. Dong, Acta Mater. **196**, 690 (2020).
55 W. H. Wang, J. Appl. Phys. **111**, 123519 (2012).
56 B. Zang, L. Song, R. Parsons, J. Shen, M. Gao, Y. Zhang, J. Huo, Y. Sun, F. Li, K. Suzuki, J.-Q. Wang, and W. Wang, Sci. China-Phys. Mech. Astron. **66**, 256111 (2023).
57 Y. Zhao, B. Shang, B. Zhang, X. Tong, H. Ke, H. Bai, and W. H. Wang, Sci. Adv. **8**, eabn3623 (2022).
58 R. Androsch, C. Schick, and J. W. P. Schmelzer, Eur. Polym. J. **53**, 100 (2014).
59 A. S. Abyzov, V. M. Fokin, N. S. Yuritsyn, M. L. F. Nascimento, J. W. P. Schmelzer, and E. D. Zanotto, J. Chem. Phys. **158**, 064501 (2023).
60 P. Charbonneau, J. Kurchan, G. Parisi, P. Urbani, and F. Zamponi, Nat. Commun. **5**, 3725 (2014).
61 P. G. Debenedetti, and F. H. Stillinger, Nature **410**, 259 (2001).
62 W. Chu, Z. Wang, N. Ren, B. Dong, J. Yu, P. Guan, Y. Liu, Y. Yue, and L. Hu, Sci. China-Phys. Mech. Astron. **66**, 246112 (2023).
63 C. Zhang, L. Hu, Y. Yue, and J. C. Mauro, J. Chem. Phys. **133**, 014508 (2010).
64 L. Xue, L. Shao, Q. Luo, L. Hu, Y. Zhao, K. Yin, M. Zhu, L. Sun, B. Shen, and X. Bian, J. Mater. Sci. Tech. **77**, 28 (2021).
65 L. Hu, and Y. Yue, J. Phys. Chem. C **113**, 15001 (2009).
66 Y. Yue, J. Non-Cryst. Solids-X **14**, 100099 (2022).
67 J. Shen, H. P. Zhang, Z. Q. Chen, L. F. Ouyang, F. R. Wang, Z. Lu, M. Z. Li, Y. H. Sun, H. Y. Bai, and W. H. Wang, Acta Mater. **244**, 118554 (2023).
68 J. Shen, S. L. Liu, Y. H. Sun, and W. Wang, Natl. Sci. Open **2**, 20220049 (2023).
69 F. Zhu, S. Song, K. M. Reddy, A. Hirata, and M. Chen, Nat. Commun. **9**, 3965 (2018).
70 J. Gu, M. Song, S. Ni, S. Guo, and Y. He, Mater. Des. **47**, 706 (2013).